



OPEN ACCESS

EDITED BY

Yi Wang,
Sichuan Academy of Medical Sciences and
Sichuan Provincial People's Hospital, China

REVIEWED BY

David Peter Al-Adra,
University of Wisconsin-Madison,
United States
Nan Zhang,
The Ohio State University, United States

*CORRESPONDENCE

Bart M. Vanaudenaerde
✉ bart.vanaudenaerde@kuleuven.be

RECEIVED 12 January 2024

ACCEPTED 25 March 2024

PUBLISHED 25 April 2024

CITATION

Heigl T, Kaes J, Aelbrecht C, Serré J, Yamada Y, Geudens V, Van Herck A, Vanstapel A, Sacreas A, Ordies S, Frick A, Saez Gimenez B, Van Slambrouck J, Beeckmans H, Acet Oztürk NA, Orlitova M, Vaneylen A, Claes S, Schols D, Vande Velde G, Schupp J, Kaminski N, Boesch M, Korf H, van der Merwe S, Dupont L, Vanoirbeek J, Godinas L, Van Raemdonck DE, Janssens W, Gayan-Ramirez G, Ceulemans LJ, McDonough JE, Verbeken EK, Vos R and Vanaudenaerde BM (2024) The nature of chronic rejection after lung transplantation: a murine orthotopic lung transplant study. *Front. Immunol.* 15:1369536. doi: 10.3389/fimmu.2024.1369536

COPYRIGHT

© 2024 Heigl, Kaes, Aelbrecht, Serré, Yamada, Geudens, Van Herck, Vanstapel, Sacreas, Ordies, Frick, Saez Gimenez, Van Slambrouck, Beeckmans, Acet Oztürk, Orlitova, Vaneylen, Claes, Schols, Vande Velde, Schupp, Kaminski, Boesch, Korf, van der Merwe, Dupont, Vanoirbeek, Godinas, Van Raemdonck, Janssens, Gayan-Ramirez, Ceulemans, McDonough, Verbeken, Vos and Vanaudenaerde. This is an open-access article distributed under the terms of the [Creative Commons Attribution License \(CC BY\)](https://creativecommons.org/licenses/by/4.0/). The use, distribution or reproduction in other forums is permitted, provided the original author(s) and the copyright owner(s) are credited and that the original publication in this journal is cited, in accordance with accepted academic practice. No use, distribution or reproduction is permitted which does not comply with these terms.

The nature of chronic rejection after lung transplantation: a murine orthotopic lung transplant study

Tobias Heigl ¹, Janne Kaes ¹, Celine Aelbrecht¹, Jef Serré ¹, Yoshito Yamada ^{1,2}, Vincent Geudens ¹, Anke Van Herck ¹, Arno Vanstapel ^{1,3}, Annelore Sacreas ¹, Sofie Ordies ¹, Anna Frick¹, Berta Saez Gimenez ^{1,4}, Jan Van Slambrouck ¹, Hanne Beeckmans ¹, Nilüfer A. Acet Oztürk ^{1,5}, Michaela Orlitova ¹, Annemie Vaneylen¹, Sandra Claes ³, Dominique Schols ³, Greetje Vande Velde ⁶, Jonas Schupp ^{7,8}, Naftali Kaminski ⁷, Markus Boesch ⁹, Hannelie Korf ⁹, Schalk van der Merwe ^{9,10}, Lieven Dupont ¹, Jeroen Vanoirbeek ¹, Laurent Godinas ¹, Dirk E. Van Raemdonck ¹, Wim Janssens ¹, Ghislaine Gayan-Ramirez ¹, Laurens J. Ceulemans ¹, John E. McDonough ^{1,7}, Erik K. Verbeken ³, Robin Vos ¹ and Bart M. Vanaudenaerde ^{1*}

¹Laboratory of Respiratory Diseases and Thoracic Surgery, KU Leuven and UZ Gasthuisberg, Leuven, Belgium, ²Department of Thoracic Surgery, Kyoto University Hospital, Kyoto, Japan, ³Translational Cell and Tissue Research, KU Leuven and UZ Gasthuisberg, Leuven, Belgium, ⁴Pulmonology Service, Lung Transplant Program, Hospital Universitari Vall d'Hebrón, Barcelona, Spain, ⁵Department of Respiratory Medicine, Uludag University Faculty of Medicine, Bursa, Türkiye, ⁶Department of Imaging and Pathology, Biomedical MRI/MoSAIC, KU Leuven, Leuven, Belgium, ⁷Pulmonary, Critical Care and Sleep Medicine, Yale University School of Medicine, New Haven, CT, United States, ⁸Department of Respiratory Medicine, Hannover Medical School and Biomedical Research in End-stage and Obstructive Lung Disease Hannover, German Lung Research Center (DZL), Hannover, Germany, ⁹Laboratory of Hepatology, CHROMETA Department, KU Leuven, Leuven, Belgium, ¹⁰Department of Gastroenterology and Hepatology, UZ Leuven, Leuven, Belgium

Introduction: Chronic rejection is a major complication post-transplantation. Within lung transplantation, chronic rejection was considered as airway centred. Chronic Lung Allograft Dysfunction (CLAD), defined to cover all late chronic complications, makes it more difficult to understand chronic rejection from an immunological perspective. This study investigated the true nature, timing and location of chronic rejection as a whole, within mouse lung transplantation.

Methods: 40 mice underwent an orthotopic left lung transplantation, were sacrificed at day 70 and evaluated by histology and in vivo μ CT. For timing and location of rejection, extra grafts were sacrificed at day 7, 35, 56 and investigated by ex vivo μ CT or single cell RNA (scRNA) profiling.

Results: Chronic rejection originated as innate inflammation around small arteries evolving toward adaptive organization with subsequent end-arterial fibrosis and obliterans. Subsequently, venous and pleural infiltration appeared,

followed by airway related bronchiolar folding and rarely bronchiolitis obliterans was observed. Ex vivo μ CT and scRNA profiling validated the time, location and sequence of events with endothelial destruction and activation as primary onset.

Conclusion: Against the current belief, chronic rejection in lung transplantation may start as an arterial response, followed by responses in venules, pleura, and, only in the late stage, bronchioles, as may be seen in some but not all patients with CLAD.

KEYWORDS

lung transplantation, chronic rejection, imaging, single-cell profiling, mouse model

Introduction

Lung transplantation is a life-saving treatment for end-stage lung diseases. However, the lung is prone to rejection due to the strong allo-immune response of the specialized mucosal immune barrier of the lung epithelium. Rejection represents the Achilles' heel of lung transplantation, with a survival rate below that of other solid organ transplantations (5-year survival of 59%) (1). Transplant immunologists have classified rejection into three stages depending on the timing post-transplant: hyperacute, acute, and chronic rejection (2), occurring within the first hours, weeks, or more than 6 months after transplantation. Chronic rejection involves cellular and humoral immune activation, is poorly responsive to treatment, and consequently is the main culprit for long-term survival (2). The clinical presentation of chronic rejection is a gradual late allograft dysfunction in which other causes such as infection and malignancy are excluded (3). Pathologically, chronic rejection in organ transplantation is characterized by vascular intimal thickening and fibrosis, resulting in graft necrosis, atrophy, and loss of functionality. In lung transplantation, the destruction of only small airways, pathologically termed obliterative bronchiolitis (OB), was considered the manifestation of chronic rejection (4). Chronic rejection is presumed to be the immunological counterpart of the clinical concept of chronic lung allograft dysfunction (CLAD), uniting all late persisting lung function deteriorations without identifiable cause (3, 5). Understanding how the immunological concept of "specific" rejection fits into the clinical concept of "non-specific" CLAD

[bronchiolitis obliterans syndrome (BOS) and restrictive allograft syndrome (RAS)] is essential in determining the true nature of clinical rejection, resulting in better patient management and outcome.

The mouse orthotopic left lung transplant model based on the cuff technique (6, 7) is a unique way to study rejection. This model involves all essential elements to properly study lung transplant rejection "in a controlled way", as it includes the lung as a functioning organ, an immune response responding against an MHC (H2) mismatch, the role of immunosuppression on the lung "architecture", and immune system, and "secondary immunodeficiency". Reports on chronic rejection in orthotopic lung transplantation mostly involved a minor mismatch setting without immunosuppression (8–10); however, we developed a unique model of chronic rejection combining a major genetic mismatch with daily immunosuppression (11, 12).

Our aim was to document the true nature of the immune system "rejecting" the foreign donor lung within a controlled mouse lung transplant setting. This study addresses the timing, the location, and the different elements of the immune system (innate and adaptive) and lung (airways, vessels, parenchyma, and pleura) changes during chronic rejection by using histology, *in vivo* and *ex vivo* μ CT imaging, and single-cell RNA profiling.

Methods

Mouse orthotopic left lung transplantation

All mice received human care in compliance with the European Convention on Animal Care and the *Guide for the Care and Use of Laboratory Animals* published by the National Institutes of Health (NIH publication 86-23, 1996). The study was approved by the Ethics Committee for Animal Research at KU Leuven (P008/2017). Male C57BL/6/N and BALB/C mice, 10–12 weeks old, were purchased from Janvier Labs (France). Orthotopic left lung transplantation was performed as described by Jungraithmayr et al. (7). In summary, following thoracotomy, the artery, vein,

Abbreviations: A, Allograft; BOS, Bronchiolitis obliterans syndrome; CXCR3, Chemokine CXC receptor 3; CXCL14, Chemokine CXC ligand 14; CLAD, Chronic lung allograft dysfunction; ECM, Extracellular matrix; FBS, Fetal bovine serum; FcR, Immunoglobulin receptor; HU, Hounsfield units; H&E, Hematoxylin–eosin; I, Isograft; Ig, Immunoglobulin; ILD, Interstitial lung disease; μ CT, Microcomputed tomography; MHC, Major histocompatibility complex; MT, Masson trichrome; OB, Obliterative bronchiolitis; PGD, Primary graft dysfunction; RAS, Restrictive allograft dysfunction; Treg, Regulatory T lymphocyte.

and bronchus were separated from each other, and 10-0 ligatures were placed around the structures. The pulmonary artery and pulmonary vein were closed using 9.0 sutures. First, the vein was anastomosed, followed by the artery, and finally the bronchus. The sutures were released and the lung was inflated. Hereafter, the chest was closed, and the animals were placed on a heating pad after waking up.

Post-transplant study design

A total of 80 mice, consisting of 52 C57BL6/NRj and 28 BALB/cJrj mice, were used. In total, 28 left lung allografts from BALB/c donor mice were transplanted into C57BL/6N recipients. Twelve isograft transplantations were performed with C57BL/6N donor lungs in C57BL/6N recipients as controls. All mice received daily maintenance immunosuppression subcutaneously, consisting of cyclosporine (10 mg/kg/d CsA; Novartis, Belgium) and steroids (1.0 mg/kg/d or 1.6 mg/kg/d methylprednisolone; Pfizer, Belgium). The low dose of steroids is equivalent to the human situation, and the high dose corresponds to other mouse models considering the higher metabolism of mice (11, 12).

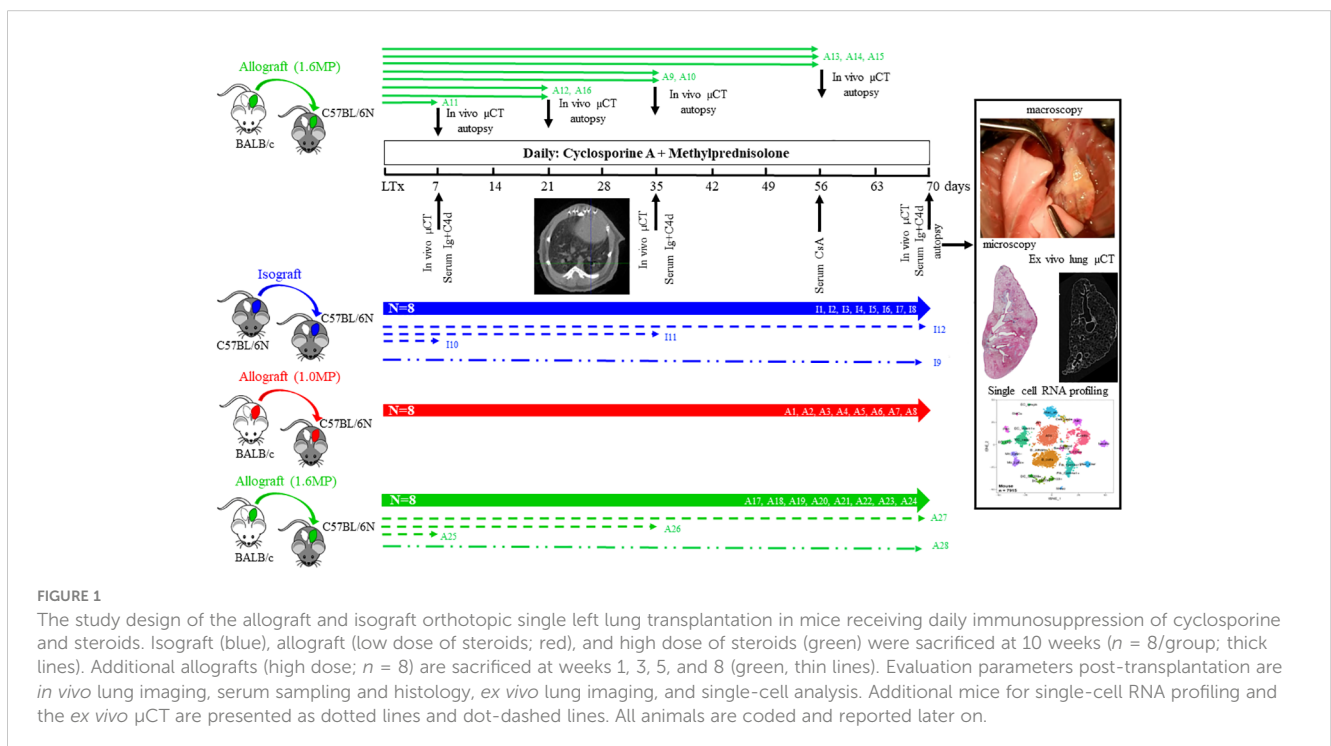
In the first set of transplantations, 16 allografts and 8 isografts were monitored daily until sacrifice (day 70). The 8 isografts (I1–I8) and the first 8 allografts received an immunosuppression regimen of CsA with low steroids (A1–A8) ($n = 8$), while the second 8 allografts received CsA with high steroids (A17–A24). The follow-up included the following: daily body weight monitoring, cyclosporine measurement in the blood (retro-orbitally bleeding) at day 56, blood sampling to measure immunoglobulins and complement, and *in vivo* μ CT imaging at days 7, 35, and 70 (Figure 1). At sacrifice, a video of the ventilating lung was

recorded to document the lung functionality. The macroscopic status of the lungs was classified as failure, extreme deformation, severe deformation, and mild changes (Figure 2). A failed lung had shrunken and was non-ventilating, with or without attachment to the thoracic wall. Within extremely deformed lungs, the lung structures (vessels, airways, and parenchyma) could not be discriminated against anymore, and only a hard, solid fibrotic mass was observed on histology. Within severe deformation, lung structures could still be identified, but no ventilation of the lung was seen. Macroscopically, mildly rejecting lungs were still ventilating and had a normal volume and normal surface appearance (Figure 3, Supplementary Figure S3). In a second group of eight allografts receiving CsA and high steroids, mice were sacrificed earlier to investigate the macroscopic changes and microscopic presentation of the early μ CT. Allografts were sacrificed at day 7 (A11; $n = 1$), day 21 (A12 and A16; $n = 2$), day 35 (A9 and A10; $n = 2$), and day 56 (A13–A15; $n = 3$).

A last set of transplantations of three isografts (I10–I12) and three allografts (A25–A27) were sacrificed at days 7, 35, and 70, and the transplanted lungs were used for single-cell RNA sequencing. One healthy/untreated BALB/cJrj and one healthy/untreated C57BL/6NRj left lung were used as baseline controls. Finally, for *ex vivo* imaging, one isograft (I9) and one allograft (A28) were sacrificed at day 70. An overview of the mice and methodology is presented in Figure 1.

Longitudinal *in vivo* μ CT imaging

To evaluate the left transplanted lung during follow-up, *in vivo* μ CT imaging (days 7, 35, and 70) was performed with a small-animal μ CT scanner (SkyScan 1278, Bruker, Belgium; resolution =



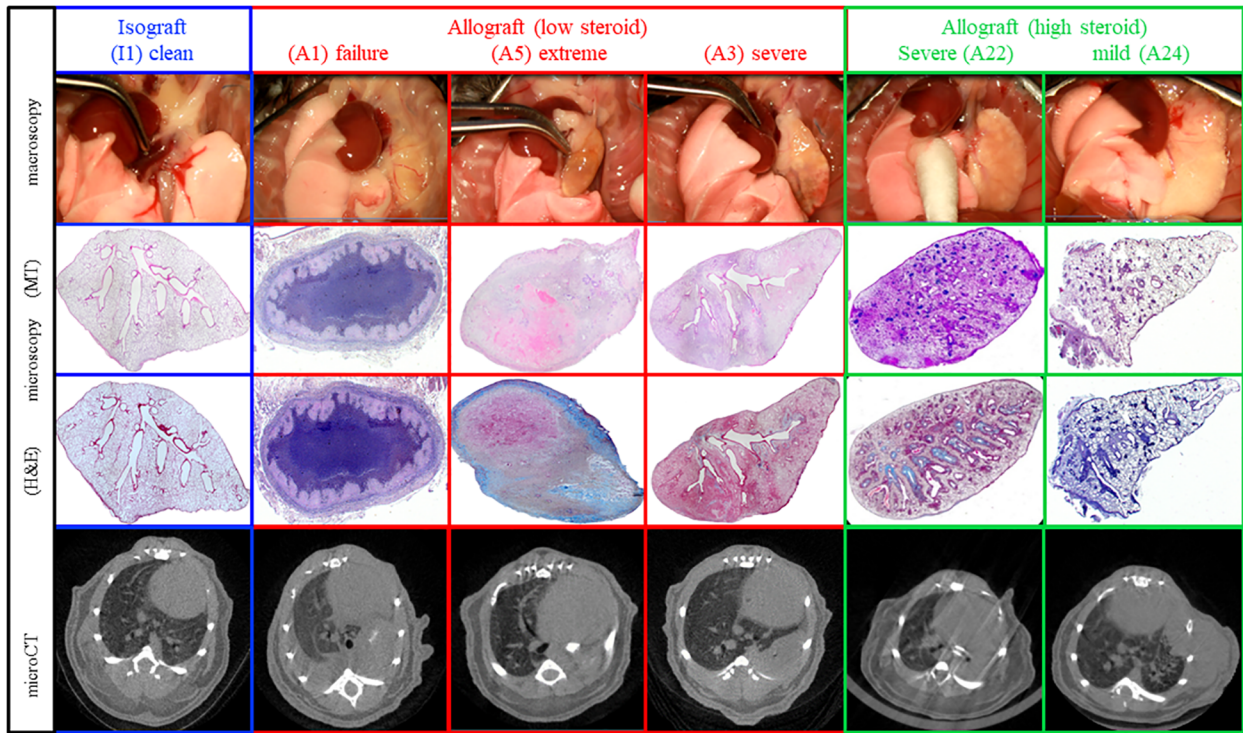


FIGURE 2
Representative macroscopy, microscopy, and *in vivo* μ CT of the different pathological presentations at day 70. The different patterns include fully normal lungs, completely destroyed failures, and lungs demonstrating chronic rejection with a spectrum of extreme, severe, and mild rejection.

55 μm^3). Mice were anesthetized, and respiratory-gated μ CT images of free-breathing animals were acquired. The respiratory cycle was divided into four phases, from the initiation of inspiration to end expiration, and scan parameters were described previously (13) (14)

to quantify lung volume and mean lung density for a manually delineated volume of interest (VOI) on the transversal μ CT images at end expiration (15). The left transplanted and right native control lungs were analyzed separately to investigate their changes properly.

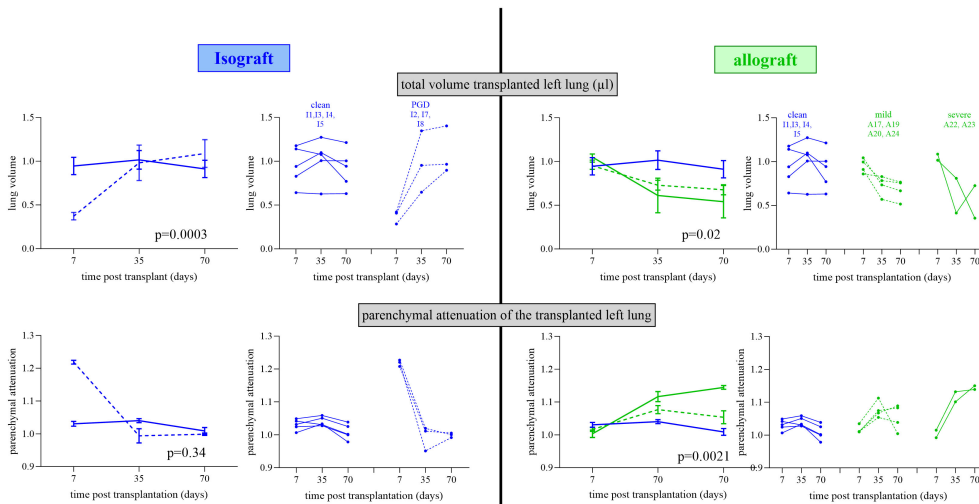


FIGURE 3
Repeated *in vivo* μ CT lung evolution of the isograft and allograft groups. *In vivo* μ CT lung evolution for lung volume and parenchymal attenuation. μ CT parameters are normalized to the reference lungs. The left side shows the isografts (blue lines) stratified according to the occurrence of PGD (dotted line) or not (full line) with group variation and individual evolution. The right side shows isografts (no PGD; blue) and allografts (green) stratified according to mild (dotted line) and severe (full line) rejection with group variation and individual evolution. For group variation, the median with SEM is presented at each time point.

To make the data comparable, untreated C57BL/6N ($n = 4$) and BALB/c ($n = 4$) littermates were scanned to create baseline values. Owing to the anatomical differences in lung structure and volume, transplanted lungs of isografts were normalized using C57BL/6N baseline data, and transplanted lungs of allografts were normalized using BALB/c baseline data.

Lung histopathology

Lungs were fixed (10% formalin, 24 h) and paraffin sections (7 μm) were stained with hematoxylin–eosin (H&E) and Masson trichrome (MT), and sections were evaluated by a pathologist to identify the pathological elements of chronic rejection. To observe how lung structural changes parallel the organization of the immune system, mice were sacrificed at different time points to find a sequence of events with respect to lung architecture, as performed previously (11, 12).

Ex vivo μCT

One isograft (I9) and one mildly rejecting allograft (A28) lung collected at day 70 were used for *ex vivo* μCT to reconstruct the early changes in an allograft. The grafted lung was fixated (10% formalin; 24 h), followed by ethanol dehydration (70%/80%/90%/100%) and complete chemical drying in hexamethyldisilazane. Dried lungs were scanned using an *ex vivo* SkyScan 1272 μCT scanner (resolution = 2.5 μm ; Bruker) to segment the airway, veins, and arterial lumen by ITK-SNAP (16).

Blood analysis

Cyclosporine blood levels were analyzed with an immunoassay (Dimension[®] RXL, Diamond Diagnostics, USA). Serum immunoglobulins (IgG/IgE/IgM/IgG1/IgG2b/IgG2c/IgG3) were measured with a ProcartaPlex Mouse Isotyping Panel (Thermo Fisher, Belgium). Serum complement factor 4d was measured by the conventional ELISA kit C4d (MyBioSource, USA).

Single-cell RNA sequencing

Grafted lungs from three isografts (I10–I12) and three allografts (A25–A27) at days 7, 35, and 70 were excised and immediately processed into single-cell suspension according to the Miltenyi protocol (Miltenyi Lung Dissociation Kit mouse). One BalBc lung was included as a comparison. Single-cell suspensions of the left lung of seven mice (control BALB/c, $n = 1$; isografts at days 7 and 70, $n = 1$ per time point; allografts at days 7, 35, and 70, $n = 1$ per time point) were successfully obtained. Briefly, the lungs were flushed, excised, and cleaned of excess tissue. The MACS enzyme solution was instilled into the lung, and the lobes were transferred into gentle MACS tubes containing the enzyme mix to dissociate cells. Single-cell suspensions were cryopreserved in liquid nitrogen until sequencing. Single-cell

RNA sequencing was performed using the 10x Genomics 3-prime-v3 dual index assay using the manufacturer's protocol. Sequencing was performed using an Illumina HiSeq4000. Read alignment was made as previously published (17) using the mouse genome (GRCm39). The gene-cell matrix was inputted into Seurat (v4.0.3) for analysis. The matrix was filtered to remove cells with <1,000 reads or >5% mitochondrial genes, normalized, and scaled with a regression of mitochondrial gene percentage. Clusters were grouped using Louvain clustering, and cell-type clusters were determined using canonical marker genes and FindAllMarkers to identify uniquely expressed genes based on their expression of these marker genes. Cells were then classified into epithelial, endothelial, stromal, and immune groups based on their type. UMAP reduction was used for visualization. Differentially expressed genes were identified using the FindMarkers set to compare allograft time points (e.g., A1W) with all other groups. GO enrichment analysis was performed with *clusterProfiler* (v3.18.0) (18). Up- and downregulated genes of allografts compared to isografts and controls were identified using the *FindMarkers* function in *Seurat* (expression in at least 10% of cells, adjusted p -value < 0.05, and average log₂ fold change < -0.25 or >0.25). GO enrichment analysis was performed using *enrichGO* with default parameters and the *org.Mm.eg.db* (v3.12.0). *Revigo* and *simRel* were used to summarize GO ontology terms (19). Adjusted log₁₀ p -values were visualized using *ggpubr* (v0.4.0). Connectome analysis was performed using the Connectome (v1.0.0) package on github (<https://msraredon.github.io/Connectome/>). Default parameters were used with the exception of setting the minimum Z -score to 2.6 for visualization. Cellular archetypes were identified with pseudotime analysis using the *phateR* (v1.0.7) and *slingshot* (v1.8.0) packages in R to determine cells that show correlated or unique features with disease progression. The visualization of heatmaps was done using *ComplexHeatmap* (v2.6.2).

Statistics

Data analysis was performed with Prism10 (GraphPad, USA) and expressed as the mean (\pm SEM). The D'Agostino and Pearson normality test was performed. To compare the different groups, a one-way analysis of variance (ANOVA) was used, and to compare different groups over time, a mixed-effects model with Tukey's multiple comparisons post-hoc test was used. A Mann–Whitney U test was performed to compare the different transplant groups and time effects. A value of 0.05 was considered significant.

Results

Macroscopic and microscopic evaluation of the lung grafts

Macroscopic evaluation of the transplanted lungs revealed differences across and within different groups (Figure 2, Supplementary Figure S1). Evaluation of the 24 transplanted lungs at day 70 revealed five failures, including one isograft (I6), two allografts with low steroid (A2 and A8), and two allografts with

high steroid (A18 and A21). Failures histologically presented necrosis destroying the lung, including parenchyma, airways, and vessels. In three of the graft failures (I6, A1, and A8), an end-stage fibrotic mass with few cells was the only remaining fragment of the lung. To properly study chronic rejection, failures were excluded from further analysis. Macroscopically, all isografts had a normal lung color and morphology and were ventilated well. Within the low-steroid allografts, three allografts showed extreme deformation (A1, A4, and A6), and three allografts showed severe deformation (A3, A5, and A7). Within the high-steroid group, two allografts (A22 and A23) were severely deformed, while four allografts (A17, A19, A20, and A24) were mildly affected. Within the allografts, only mild rejecting allografts were ventilating at day 70 (Supplementary Figure S1). There were no differences in body weight ($p = 0.92$) and cyclosporine levels ($p = 0.35$) between the three groups (Supplementary Figure S2). The cyclosporine level of all mice was $587 \pm 35 \mu\text{g/L}$. Microscopic evaluation supported the macroscopic observation (Figure 4). Macroscopically, extreme deformation within the low-steroid allografts (A2, A4, and A6) was presented as intense end-stage fibrosis in all compartments. Although the vessels and airways could be located, these were never functional.

In vivo repeated μCT evaluation

Evaluation of lung volume changes showed differences within isografts and allografts over time ($p < 0.0001$) (Figure 5). Lung volume at day 7 was comparable between allografts and isografts. Over time, isografts showed an increasing lung volume, while allografts decreased. Changes in lung volume were observed between mildly and severely affected allografts versus clean isografts ($p = 0.025$), as mildly and severely rejected allografts had volume reductions at day 35 ($p = 0.12$ and $p = 0.39$) and day 70 ($p = 0.18$ and $p = 0.40$) versus isografts (Figure 5). The lung volume difference between inspiration and expiration on μCT scans (a type of tidal volume) was compromised in allografts and was greatly

compromised in severely rejecting allografts. Analysis of the right native lung confirmed that the decrease in tidal volume was caused by the graft (Supplementary Figure S3). Parenchymal attenuation of the transplanted lung was different ($p < 0.0001$) between isografts and allografts. Allografts were initially open (day 7) and lung attenuation appeared afterwards (Figure 6). Attenuation was increased in mild and severe rejecting allografts at day 35 ($p = 0.087$ and $p = 0.036$) and day 70 ($p = 0.15$ and $p = 0.0002$) versus isografts. Low-steroid allografts had more attenuation than high-steroid allografts at days 35 and 70 ($p = 0.0011$ and 0.009). The native lung had no increased attenuation, confirming the absence of collateral damage or possible infection (Supplementary Figure S4). Isografts demonstrated a normal lung appearance without attenuation at day 70, but at day 7, some isografts demonstrated attenuation and resembled potential primary graft dysfunction (PGD) (Figure 3). PGD is a type of severe lung injury that occurs within the first 72 h of lung transplantation and is the most common cause of early mortality. PGD decreased towards days 35 and 70. PGD is a graft defect. Repeated μCT revealed lung volume differences between isografts with and without PGD ($p = 0.0003$). While the lung volume in PGD was lower at day 7, it returned to the level of the isografts without PGD at days 35 and 70 (Figure 3).

Pathological pattern of chronic rejection in time and space

Pathological examination of allografts under high immunosuppression revealed an evolutionary pattern of chronic rejection organized by time, location, and immune response (Figure 7). Stage 1, shown in an allograft (A11, day 7), presented neutrophil extravasation into the vessel wall of end-arterioles, reducing the arteriolar lumen without increasing wall thickness. Stage 2 showed inflammation around end-arterioles and end-venules. The innate activation around end-arterioles increased in

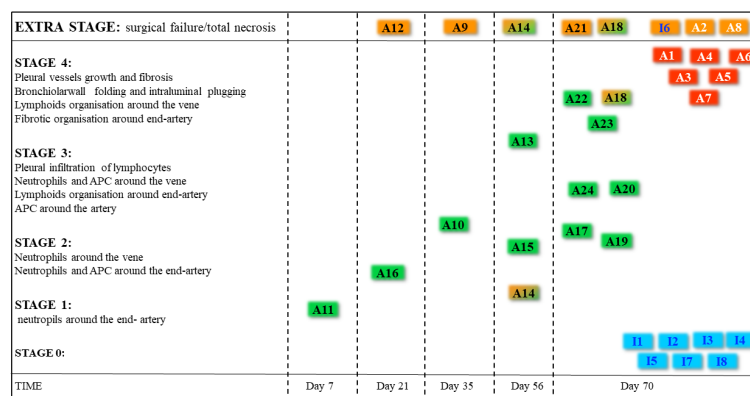


FIGURE 4

The pathological staging of rejection. All allografts were used to identify the stage and were subdivided into stages of rejection. Failures are documented in orange boxes. Two animals demonstrated a part of the lung to be destroyed, and another part presented rejection (half green half orange boxes). The color of the boxes in the included lungs represents the origin of the graft being an isograft (blue, $n = 7$), an allograft under high-dose steroids (green boxes, $n = 13$), and an allograft under low-dose steroids (red boxes, $n = 6$).

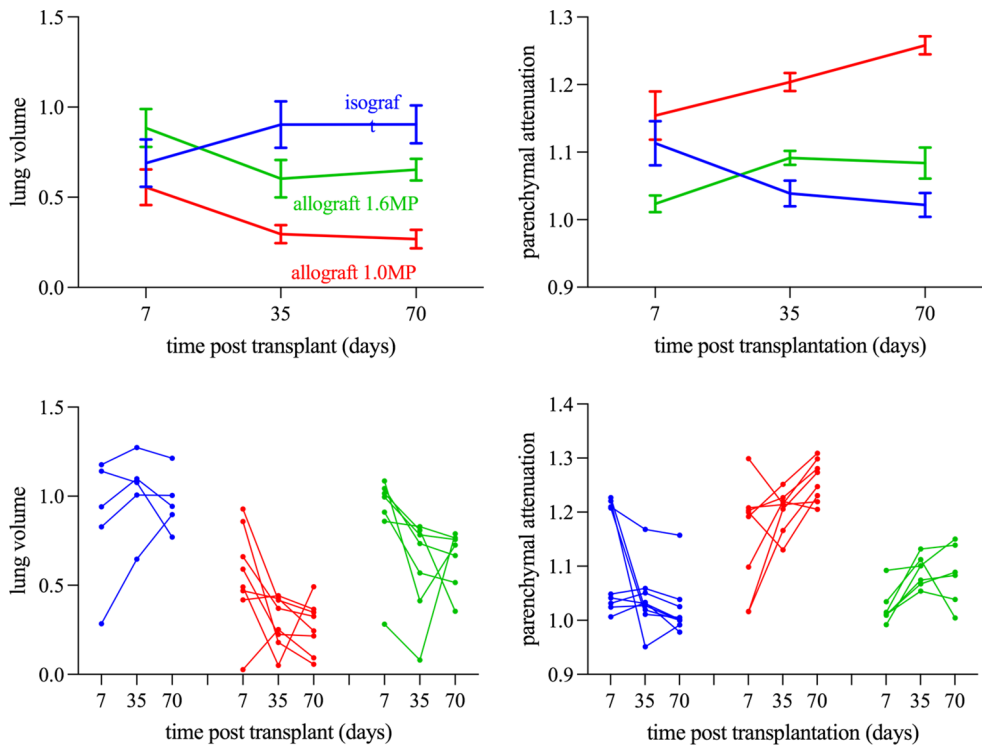


FIGURE 5 Longitudinal morphometric μ CT analysis stratified according to the severity of rejection (Tx left lung). **(A)** Total lung volume of the transplanted left lung. **(B)** Parenchymal attenuation of the transplanted left lung. The Left shows the isograft group (blue lines) stratified according to the occurrence of PGD (dotted lines). The right shows the Allograft 1.6MP group (green lines) stratified according to the severity of rejection (mild rejection is denoted as dotted lines and severe rejection is denoted as full lines). All data have been normalized as described in the Methods section.

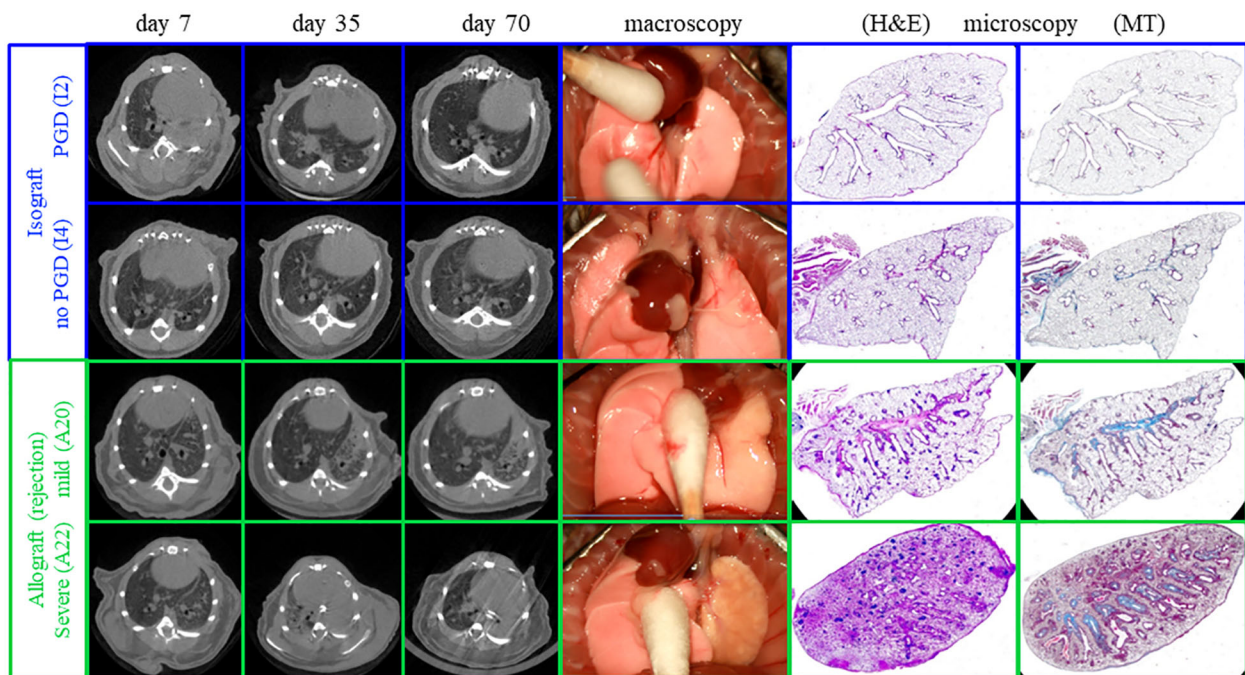


FIGURE 6 Representative macroscopy, microscopy, and *in vivo* μ CT imaging of mild and severe chronic rejection. One allograft with mild rejection and one with severe rejection are presented (green). In comparison, a control isograft is present, and an additional isograft demonstrating on μ CT at week 1 primary graft dysfunction (PGD).

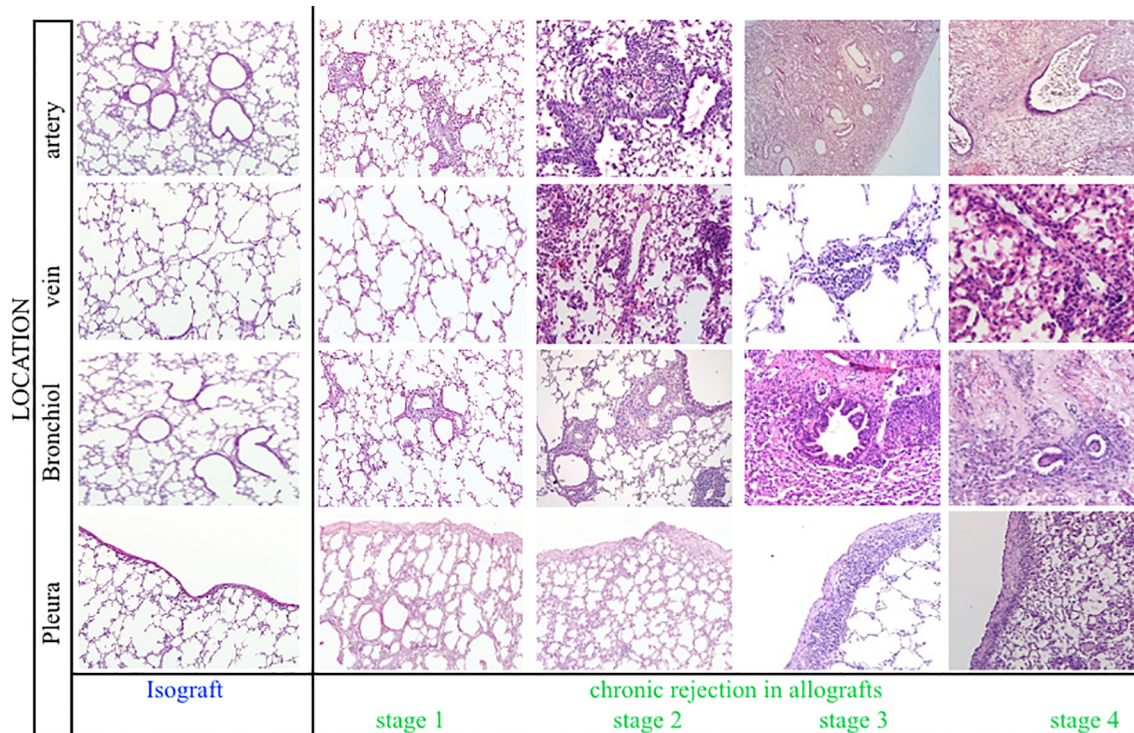


FIGURE 7
 Representative histological illustrations of the four stages of chronic rejection. For each stage, the different anatomical lung compartments involved were presented, including arteries, veins, bronchioles, and pleura. Stage 1, Stage 2, Stage 3, and Stage 4 are represented by A11 at day 7, A16 at day 21, A24 at day 70, and A22 at day 70, respectively.

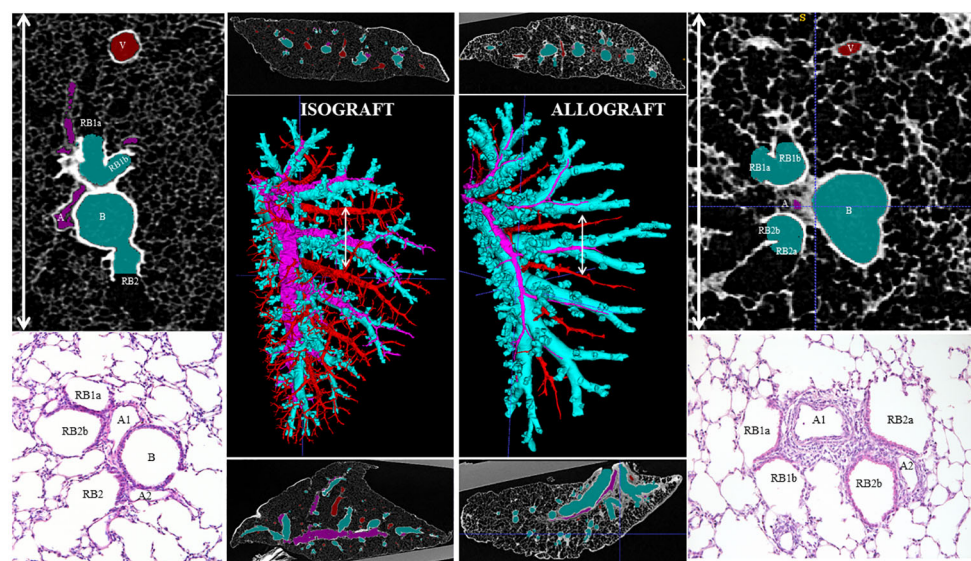


FIGURE 8
 An *ex vivo* high-resolution μ CT imaging and reconstruction of the organization of chronic rejection. The airways (light blue), arterial vessels (pink), and venous vessels (red) of the transplanted left lung were segmented and reconstructed in 3D (middle large picture) in an isograft (left) and an allograft (right). A transverse and sagittal image of the scans is presented above and below the reconstruction. On the right and left sides of the figure, μ CT (top) and histological (bottom) details of the broncho-vascular bundle, specifically of the location of the white arrow line, identify the arterial origin of rejection at the generation where airways go over in respiratory bronchioles.

size with the influx of antigen-presenting cells. Simultaneously, neutrophils infiltrated the end-venules, but the bronchioles were still not involved. *Ex vivo* μ CT confirmed the vessel lumens narrowing for both arteries and veins, while the airway lumen remained unaffected (Figure 8, Supplementary Figure S5). Evolution toward Stage 3 consisted of immune organization

around arteries evolving toward adaptive activation. Venules remained innate, but monocytes appeared besides neutrophils. The lumen of the venules decreased, and the pleural compartment started to be infiltrated by lymphocytes. The final stage of rejection (Stage 4) of arterioles evolved toward fibrosis with end-arterial obliterans. The venous compartment remained

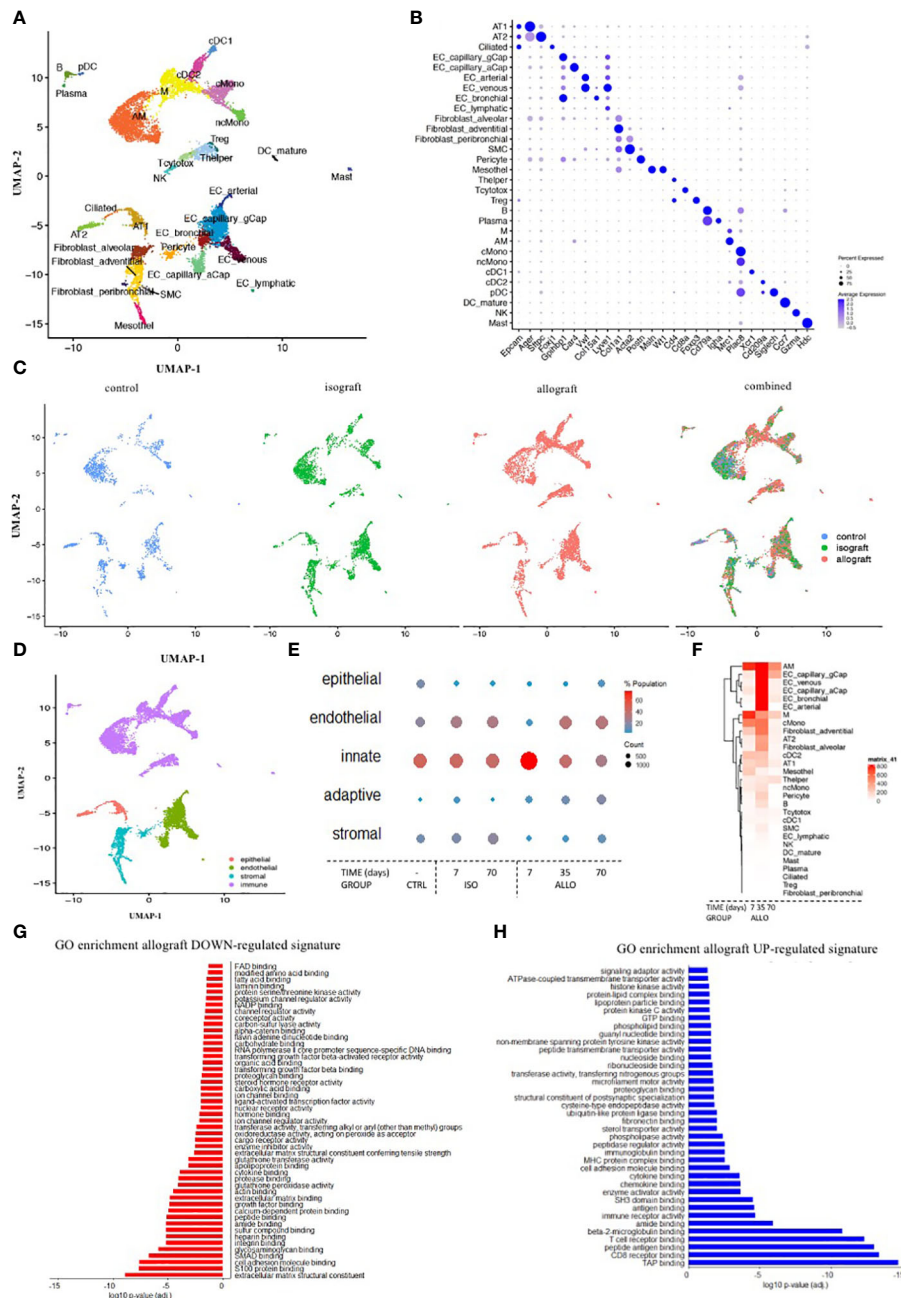


FIGURE 9
Single-cell RNA profiling to validate the sequence of chronic rejection across the different cells involved and subcellular mechanisms. (A) UMAP plot of the cells from the left lung of three isografts (7, 35, and 70 days), three allografts (7, 35, and 70 days), and one control BalBc lung color-coded by major cellular lineage. (B) Dot plot heatmap of the expression of representative marker genes of cellular lineages. The size and color intensity of each dot represent, respectively, the percentage or average expression of the marker gene in this cell type. Color scale: blue, high expression; white, low expression. (C) UMAP plot of lung cells, color-coded for the indicated conditions of the left lung. (D) UMAP plot of lung cells, color-coded for the indicated major cell subcluster. (E) Dot plot heatmap of the major cell subcluster. The size and color intensity of each dot represent, respectively, the total number and percentage of cells within each cell type. Color scale: red, high expression; blue, low expression. (F) Gene expression heatmap of all individual genes in every identified cell type. Color scale: red, high expression; blue, low expression. (G, H) A barplot of the GO enrichment analysis of down- and upregulated gene signatures in allograft lungs.

innately immune-organized, and bronchioles affected by the neighboring arteriolar inflammation demonstrated typical bronchiolar folding, but only one allograft presented fibrotic intraluminal plugging (bronchiolitis obliterans).

Single-cell RNA profiling to validate the sequence of chronic rejection

Single-cell profiling sequenced 12,821 cells from seven mice. Each specific cell within control, isograft, and allograft lungs was presented in a UMAP plot and gene marker validation (Figures 9A-C). The different cell types were clustered into structural epithelial/endothelial, innate, adaptive, and stromal cells (Figures 9D, E). The structural cells decreased at day 7 in allografts compared to isografts and controls and recovered gradually at days 35 and 70 (Supplementary Figure S7C). Innate cells increased at day 7 and returned to the isograft and control levels at days 35 and 70 (Figure 9E, Supplementary Figures S7A-C). Cell profiling of eosinophils and neutrophils was unsuccessful and could not be evaluated. Adaptive cells, including T helper and cytotoxic cells, B cells, plasma B cells, and Treg cells, gradually increased toward day 70. Finally, stromal cells started to increase and eventually generated the fibrotic environment (Figure 9E) for chronic rejection. Although adventitial fibroblasts appear to be the leading producers of extracellular matrix (ECM), multiple stromal cells were upregulated.

Overall gene expression in allografts was increased versus isografts and control lungs. Endothelial cells and monocytes/macrophages showed a particular increase in gene expression, suggestive of a key role in the onset and progression of rejection (Figure 9F). Upregulation of signaling pathways linked to the immune response, with innate and adaptive elements such as MHCII elements, receptor binding, proteasome formation, and downstream signal transduction (Figure 9H), was found. In the early onset of rejection, macrophages presented an increased expression of MHCII together with CXCR3, CXCL14, and FcRE. T cell receptor-related costimulatory elements are upregulated at an early stage, even prior to the increase and proliferation of the T cells (Supplementary Figure S8D). To examine the temporal evolution of the expression, pseudotime analysis identified genes involved in early and late processes (Supplementary Figures S8E, F). Within the Tc cells, inducer and effector cytokines are increasingly expressed (Supplementary Figure S8C). ECM production was very active in the early period after transplantation and subdued at day 70 (Supplementary Figure S9D). Contractile properties are present in smooth muscle cells, whose expression levels decreased early after transplantation of isografts but recovered later (Supplementary Figure S9D). Connectome analysis confirms these complex changes of lung homeostasis and immune activation with innate cells linked to endothelial cell involvement early on and to adaptive cell involvement later on (Supplementary Figures S9E, F). GO enrichment analysis confirmed that structural cells and stromal cells have very low general gene expression. Downregulation of signaling pathways related to cell homeostasis, integrity, and organization was observed to be involved in the onset of rejection (Figure 9G). Mechanistic clues demonstrated that isografts receiving

immunosuppression had lower levels of MHC molecules in the structural cells. However, during rejection, MHC expression increased in allografts above isograft levels (Supplementary Figure S7D). These higher levels of MHCII are confirmed by the increase in proteasome elements, expression of chemokines, and interferon elements (Supplementary Figure S7E). In addition, MHCII expression was also increased, especially during the early phase of rejection.

Systemic humoral involvement

Measurements of humoral components showed large inter-individual variation, making it difficult to reach significance. IgA and IgG1 were below detection, while immunoglobulins IgG1, IgG2, and IgG3 tended to increase in severe rejection. IgG2c and IgG3 were linked to adaptive organization in late and severe rejection. IgM slightly increased early on, while IgE and C4d tended to increase in late severe rejection. Humoral activation was absent in isografts (Supplementary Figure S10).

Discussion

This orthotopic lung transplant model, including a major MHC mismatch with immunosuppression, is the first to examine the nature, timing, and place of chronic rejection after lung transplantation. The methodological approach combining imaging, histology, and transcriptomic profiling allows the observation of chronic rejection from pathology to immunology.

We revealed the true nature of chronic rejection after lung transplantation, originating around vessels and, more precisely, around the arterioles. After innate activation, adaptive activation and fibrosis around arteries resulted in end-arteritis obliterans. Only later did innate venous inflammation, pleural infiltration/fibrosis, and “obliterative bronchiolitis” appear. μ CT imaging confirmed that the gradual rejection model within 10 weeks was reproducible. The gradual onset of rejection questions the segregation of rejection into hyperacute, acute, and chronic rejection. Both cellular and humoral immunity may be part of the same immune response to rejection, where only the timing and magnitude differ.

The most important finding is the endothelial origin of chronic rejection, which alludes to abandoning the old enigma of airway-centered rejection, “obliterative bronchiolitis”. The concept that recipients’ immune cells only identify foreign cells in the small airway as “non-self” and induce the rather limited immune organization of the OB is counterintuitive. Although previous mouse lung transplant studies identified intraluminal airway fibrosis and constriction, including pleuroparenchymal infiltration and fibrosis (10, 12, 20, 21), this study identified the first site of chronic rejection as being at the arteriole site. This new observation is in line with all solid organ transplantations (22) and is more plausible as recipients’ immune cells enter the “foreign” donor via arteries, representing the first contact location.

μ CT imaging opened unique insights into the progression of rejection. Early innate onset and adaptive immune activation around the arteries and venous compartment are presented as mild lung attenuation. Severe attenuation is present when fibrotic organization around arteries, venous innate inflammation, and pleural and airway inflammation are histologically found.

Histological imaging of chronic rejection in both time and place was confirmed by single-cell RNA profiling. The earliest event of (chronic) rejection—endothelial activation—was observed by the upregulation of MHC1/2, adhesion molecules, and integrins, initiating extravasation of innate and adaptive immune cells. Within T helper cells, early master, inducer, and effector cytokines were not only increasingly expressed, demonstrating lymphoid activation, but also blocked regulation as Treg cells. Rejection is not only about immune cells controlling homeostasis but also about structural and stromal cells. Low expression levels in structural cells and stromal cells indicate that the lung structure is under pressure and its homeostasis is lost. Although adventitial fibroblasts appear to be the leading producers of ECM in rejection, multiple stromal cells were identified as ECM drivers, supporting the idea that rejection is more than restricted to OB lesions. In addition to the B cell involvement found by histology and cell profiling, humoral elements such as IgG2c and IgG3 confirmed the adaptive response in late rejection, in line with delayed-type hypersensitivity of rejection. Obviously, cell profiling should be more mechanistically validated.

This murine model, with its diagnostic tool, opens new horizons. This study maps (chronic) rejection and confirms its standard immune response nature, as we have only one immune system. Since all cells, cytokines, and so on resemble the classical immune responses, it is difficult to consider the specificity of rejection. Immune responses against microbial and malignant cells or immune responses due to secondary immune deficiency may have seriously biased our understanding of rejection. All can be studied in this controlled setting by paralleling infections, environmental factors, medication non-adherence, and autoimmune-induced immune responses. In addition, this model opens perspectives for immunotherapy research.

Limitations are the low *n*-values, the presence of failures, and the heterogeneity of rejection. To prevent failures, it is important to identify infections, twisted cuffs, and air leaks. The heterogeneity in the progression and severity of rejection may be related to surgical processes such as suturing difficulties, flushing issues, twisted cuffs, and the uptake of immunosuppression.

Our goal to validate the histological and imaging findings of rejection was achieved very elegantly and provided new avenues for research. Where chronic rejection fits into the clinical hallmarks of BOS and RAS is not clear-cut anymore, and how these mouse findings of rejection parallel the spectrum of CLAD remains to be answered. The observed lesions in the mouse are most consistent with RAS. Patients with BOS may experience early chronic rejection, but the pronounced airway pathology caused by

immunosuppression or excessive exposure through inhalation of microorganisms and pollution may be confused with rejection. BOS and RAS are different but may have more overlap than identified.

This study described the true nature, timing, and location of chronic rejection after lung transplantation in murine orthotopic lung transplantation using cutting-edge diagnostic tools and opened new horizons for research. It invites researchers to re-explore chronic rejection in the clinical setting of CLAD.

Data availability statement

The single cell RNA dataset presented in the study are deposited in the NCBI SRA bioproject, accession number PRJNA1076139: The nature of chronic rejection after lung transplantation: a murine orthotopic lung transplant study.

Ethics statement

The animal study was approved by the Ethics Committee for Animal Research at KU Leuven. The study was conducted in accordance with local legislation and institutional requirements.

Author contributions

TH: Data curation, Formal analysis, Investigation, Methodology, Writing – original draft. JK: Formal analysis, Investigation, Methodology, Writing – review & editing. CA: Formal analysis, Investigation, Methodology, Writing – review & editing. JSe: Investigation, Methodology, Writing – review & editing. YY: Formal analysis, Methodology, Writing – review & editing. VG: Methodology, Writing – review & editing, Investigation, Visualization. AH: Data curation, Formal analysis, Writing – review & editing, Investigation, Methodology. ArV: Investigation, Methodology, Writing – review & editing, Formal analysis. AS: Methodology, Writing – review & editing, Formal analysis, Investigation. SO: Methodology, Writing – review & editing, Formal analysis. AF: Investigation, Methodology, Formal analysis, Writing – review & editing. BS-G: Writing – review & editing, Data curation, Formal analysis, Visualization. JSI: Investigation, Methodology, Writing – review & editing. HB: Investigation, Methodology, Writing – review & editing, Data curation. NA: Methodology, Writing – review & editing, Visualization. MO: Methodology, Writing – review & editing, Investigation. AnV: Investigation, Methodology, Writing – review & editing. SC: Formal analysis, Methodology, Writing – review & editing, Software. DS: Methodology, Writing – review & editing, Formal analysis, Supervision, Validation. GV: Methodology, Writing – review & editing, Formal analysis, Supervision. JSc: Formal analysis, Methodology, Writing – review & editing, Data

curation, Investigation. NK: Methodology, Supervision, Writing – review & editing, Funding acquisition, Investigation, Project administration. MB: Data curation, Formal analysis, Methodology, Writing – review & editing. HK: Funding acquisition, Supervision, Writing – review & editing, Resources. SM: Methodology, Writing – review & editing, Resources, Visualization. LD: Resources, Supervision, Writing – review & editing, Project administration. JV: Methodology, Writing – review & editing, Conceptualization, Supervision. LG: Supervision, Writing – review & editing, Data curation, Methodology. DR: Methodology, Conceptualization, Data curation, Investigation, Supervision, Writing – original draft. WJ: Supervision, Writing – review & editing, Funding acquisition, Project administration, Resources. GG-R: Funding acquisition, Project administration, Supervision, Writing – review & editing, Investigation, Methodology. LC: Investigation, Methodology, Supervision, Writing – review & editing. JM: Data curation, Methodology, Software, Writing – review & editing. EV: Methodology, Conceptualization, Data curation, Investigation, Supervision, Writing – original draft. RV: Conceptualization, Funding acquisition, Supervision, Writing – review & editing. BV: Conceptualization, Data curation, Formal analysis, Funding acquisition, Investigation, Methodology, Project administration, Resources, Supervision, Validation, Visualization, Writing – original draft, Writing – review & editing.

Funding

The author(s) declare that financial support was received for the research, authorship, and/or publication of this article. BV, WJ, and GG-R are supported by KU Leuven (C16/19/005; C24/15/030). DEVR is supported by the Broere Foundation. SM and RV are Senior Clinical Research Fellows of the Research Foundation Flanders (FWO; 12G8715N) and are supported by a UZ Leuven research grant (STG15/023). JK, ArV, and VG are Junior Research Fellows of the Research Foundation Flanders (1198920N and 1102020N). SM is supported by grants from UZ Leuven (KOOR) and KU Leuven (C1 funding). GV acknowledges funding by KU Leuven IF (C24/17/061 and STG/15/024).

Conflict of interest

The authors declare that the research was conducted in the absence of any commercial or financial relationships that could be construed as a potential conflict of interest.

Publisher's note

All claims expressed in this article are solely those of the authors and do not necessarily represent those of their affiliated organizations, or those of the publisher, the editors and the reviewers. Any product that may be evaluated in this article, or

claim that may be made by its manufacturer, is not guaranteed or endorsed by the publisher.

Supplementary material

The Supplementary Material for this article can be found online at: <https://www.frontiersin.org/articles/10.3389/fimmu.2024.1369536/full#supplementary-material>

SUPPLEMENTARY VIDEO 1

Representative macroscopy, including lung ventilation, microscopy, and μ CT of the different pathological presentations. The different patterns include fully normal lungs, completely destroyed failures, and lungs demonstrating chronic rejection with a spectrum of extreme, severe, and mild rejection.

SUPPLEMENTARY FIGURE 2

Postoperative body weight and cyclosporine trough levels. The cyclosporine trough level of all mice was $587 \pm 35 \mu\text{g/L}$, within the aimed range related to a better outcome for mice.

SUPPLEMENTARY FIGURE 4

Morphometric longitudinal *in vivo* μ CT lung evolution of the native right lung for lung volume and parenchymal attenuation. At each time point, either individual values or the median with SEM are presented.

SUPPLEMENTARY VIDEO 2

Representative longitudinal *in vivo* μ CT lung reconstruction of the representative grafts. I2, I4, A20, and A22 are represented by inspiration and expiration scans, and three rotating and ventilating 3D reconstructions of the scans at 7, 35, and 70 days.

SUPPLEMENTARY VIDEO 3

Representative *ex vivo* μ CT lung reconstruction of an isograft and mild allografts. The airways (light blue), arterial (pink), and venous (red) systems of I9 and A28 (day 70) are segmented and reconstructed in 3D.

SUPPLEMENTARY FIGURE 6

Tidal volume of the different presentations of rejection. From the representative graft (I2, I4; A20 A22) the lung volume difference between in and expiration was calculated for each time point of the whole lung (upper panel), the right native lung (left side), and the left transplanted graft lung (right side). In the lower panel, a subdivision is made for PGD in the isograft group and for mild versus severe in the allograft group.

SUPPLEMENTARY FIGURE 7

Single-cell RNA profiling of the different cells of the structural cell subcluster. (A) UMAP plot of all cells of the left lung color-coded by major cellular lineage. (B) UMAP plot of the structural cells of the left lung, color-coded by the cellular subcluster of the structural cells. (C) Dot plot heatmap of the structural cell subcluster. The size and color intensity of each dot represent, respectively, the percentage of cells within each cell type. Color scale: red, high expression; blue, low expression. (D) A heatmap of the expression of mouse MHC1/2 complex H-2 genes within the endothelial cell lineages, where each line represents a specific endothelial cell and the color intensity represents the expression of the specific H2 gene. Color scale: yellow, high expression; purple, low expression. (E) Violin plots of proteasome elements, chemokines, and interferon pathway members were divided into the control mouse and isograft and allograft at days 7, 35, and 70. (F) UMAP plot of lung cells, color-coded for different adhesion molecules. Color scale: purple, high expression; grey, low expression. G/UMAP plot of lung cells for controls, isografts, and allografts, color-coded for the adhesion molecule CD34. Color scale: purple, high expression; grey, low expression.

SUPPLEMENTARY FIGURE 8

Single-cell RNA profiling of the different cells of the immune cell subcluster. (A) UMAP plot of all cells of the left lung, color-coded by major cellular subcluster. (B) UMAP plot of the immune cells of the left lung color-coded by the cellular subcluster of the immune cells. (C) Dot plot heatmap of the

immune cell subcluster. The size and color intensity of each dot represent, respectively, the percentage of cells within each cell type. Color scale: red, high expression; blue, low expression. **(D)** Violin plots of T cell activation elements specific to the T cell subcluster divided into the control mouse, isograft, and allograft at days 7, 35, and 70. **(E)** and **(G)** Heatmaps of gene expression of genes correlated with pseudotime disease progression (Pseudotime: red to blue) within innate macrophages or adaptive T cells. Gene expression was scaled and plotted from low (purple) to high (yellow) expression.

SUPPLEMENTARY FIGURE 9

Single-cell RNA profiling of the different cells of the stromal cell subcluster. **(A)** UMAP plot of all cells of the left lung, color-coded by major cellular cluster. **(B)** UMAP plot of the structural cells of the left lung, color-coded by the cellular cluster of the stromal cells. **(C)** Dot plot heatmap of the stromal cell subcluster. The size and color intensity of each dot represent, respectively, the percentage of cells within each cell type. Color scale: red,

high expression; blue, low expression. **(D)** Dot plot heatmap of expression of representative marker genes of contractility and extracellular matrix proteins for the different groups, including control, isograft, and allograft (with time points). The size and color intensity of each dot represent respectively the percentage or average expression of the marker gene in this cell type. Color scale: blue, high expression; white, low expression. **(E)** Connectome showing ligand-receptor pairs identified within control, isograft, or allograft mice. Colors denote the different cell types. **(F)** Connectome showing ligand-receptor pairs identified in the different allograft timepoints (A1W, A5W, or A10W). It should be noted that collagen ligands were highly connected in the early stages of rejection.

SUPPLEMENTARY FIGURE 10

Serial evaluation of systemic immunoglobulins and complement factors. Immunoglobulins included are IgG1, IgG2b, IgG2c, IgG3, IgM, IgA, and IgE accompanied by IgG against double stranded DNA, BL6 DNA, and BalBc DNA. For complement, C4d was used.

References

- Sayegh MH, Carpenter CB. Transplantation 50 years later - progress, challenges, and promises. *New Engl J Med.* (2004) 351:2761–6. doi: 10.1056/NEJMon043418
- Li XC, Jevnikar AM. *Transplant immunology*. Houston, USA: Wiley-Blackwell (2015). doi: 10.1002/9781119072997
- Verleden GM, Glanville AR, Lease ED, Fisher AJ, Calabrese F, Corris PA, et al. Chronic lung allograft dysfunction: Definition, diagnostic criteria, and approaches to treatment-A consensus report from the Pulmonary Council of the ISHLT. *J Heart Lung Transplant.* (2019) 38:493–503. doi: 10.1016/j.healun.2019.03.009
- Barker AF, Bergeron A, Rom WN, Hertz MI. Obliterative bronchiolitis. *N Engl J Med.* (2014) 370:1820–8. doi: 10.1056/NEJMra1204664
- Sato M, Waddell TK, Wagnetz U, Roberts HC, Hwang DM, Haroon A, et al. Restrictive allograft syndrome (RAS): a novel form of chronic lung allograft dysfunction. *J Heart Lung Transplant.* (2011) 30:735–42. doi: 10.1016/j.healun.2011.01.712
- Okazaki M, Krupnick AS, Kornfeld CG, Lai JM, Ritter JH, Richardson SB, et al. A mouse model of orthotopic vascularized aerated lung transplantation. *Am J Transplant.* (2007) 7:1672–9. doi: 10.1111/j.1600-6143.2007.01819.x
- Jungraithmayr WM, Korom S, Hillinger S, Weder W. A mouse model of orthotopic, single-lung transplantation. *J Thorac Cardiovasc Surg.* (2009) 137:486–91. doi: 10.1016/j.jtcvs.2008.10.007
- Suzuki H, Fan L, Wilkes DS. Development of obliterative bronchiolitis in a murine model of orthotopic lung transplantation. *J Vis Exp.* (2012) 65. doi: 10.3791/3947
- Oishi H, Martinu T, Sato M, Matsuda Y, Hirayama S, Juvet SC, et al. Halofuginone treatment reduces interleukin-17A and ameliorates features of chronic lung allograft dysfunction in a mouse orthotopic lung transplant model. *J Heart Lung Transplant.* (2016) 35:518–27. doi: 10.1016/j.healun.2015.12.003
- Martinu T, Oishi H, Juvet SC, Cypel M, Liu M, Berry GJ, et al. Spectrum of chronic lung allograft pathology in a mouse minor-mismatched orthotopic lung transplant model. *Am J Transplant.* (2019) 19:247–58. doi: 10.1111/ajt.15167
- De Vleeschauwer S, Jungraithmayr W, Wauters S, Willems S, Rinaldi M, Vaneylen A, et al. Chronic rejection pathology after orthotopic lung transplantation in mice: the development of a murine BOS model and its drawbacks. *PLoS One.* (2012) 7:e29802. doi: 10.1371/journal.pone.0029802
- Yamada Y, Vandermeulen E, Heigl T, Somers J, Vaneylen A, Verleden S, et al. The role of recipient derived interleukin-17A in a murine orthotopic lung transplant model of restrictive chronic lung allograft dysfunction. *Transplant Immunol.* (2016) 39:10–7. doi: 10.1016/j.trim.2016.10.001
- Berghen N, Dekoster K, Marien E, Dabin J, Hillen A, Wouters J, et al. Radiosafe micro-computed tomography for longitudinal evaluation of murine disease models. *Sci Rep.* (2019) 9:17598. doi: 10.1038/s41598-019-53876-x
- De Langhe E, Vande Velde G, Hostens J, Himmelreich U, Nemery B, Luyten FP, et al. Quantification of lung fibrosis and emphysema in mice using automated micro-computed tomography. *PLoS One.* (2012) 7:e43123. doi: 10.1371/journal.pone.0043123
- Vande Velde G, Poelmans J, De Langhe E, Hillen A, Vanoirbeek J, Himmelreich U, et al. Longitudinal micro-CT provides biomarkers of lung disease that can be used to assess the effect of therapy in preclinical mouse models and reveal compensatory changes in lung volume. *Dis Models Mechanisms.* (2016) 9(1):91–8. doi: 10.1242/dmm.020321
- Yushkevich PA, Piven J, Hazlett HC, Smith RG, Ho S, Gee JC, et al. User-guided 3D active contour segmentation of anatomical structures: Significantly improved efficiency and reliability. *NeuroImage.* (2006) 31:1116–28. doi: 10.1016/j.neuroimage.2006.01.015
- Adams TS, Schupp JC, Poli S, Ayaub EA, Neumark N, Ahangari F, et al. Single-cell RNA-seq reveals ectopic and aberrant lung-resident cell populations in idiopathic pulmonary fibrosis. *Sci Adv.* (2020) 6:eaba1983. doi: 10.1126/sciadv.aba1983
- Yu G, Wang L-G, Han Y, He Q-Y. clusterProfiler: an R package for comparing biological themes among gene clusters. *OMICS.* (2012) 16:284–7. doi: 10.1089/omi.2011.0118
- Supek F, Bošnjak M, Škunca N, Šmuc T. REVIGO summarizes and visualizes long lists of gene ontology terms. *PLoS One.* (2011) 6:e21800. doi: 10.1371/journal.pone.0021800
- Fan L, Benson HL, Vittal R, Mickler EA, Presson R, Jo Fisher A, et al. Neutralizing IL-17 prevents obliterative bronchiolitis in murine orthotopic lung transplantation. *Am J Transplant.* (2011) 11:911–22. doi: 10.1111/j.1600-6143.2011.03482.x
- Misumi K, Wheeler DS, Aoki Y, Combs MP, Braeuer RR, Higashikubo R, et al. Humoral immune responses mediate the development of a restrictive phenotype of chronic lung allograft dysfunction. *JCI Insight.* (2020) 5. doi: 10.1172/jci.insight.136533
- Libby P, Pober JS. Chronic rejection. *Immunity.* (2001) 14:387–97. doi: 10.1016/S1074-7613(01)00119-4